Whitening of odor representations by specific network connectivity

Adrian A. Wanner[1,2,3], Rainer W. Friedrich[1,2]

1 Friedrich Miescher Institute for Biomedical Research, Maulbeerstrasse 66, 4058 Basel, Switzerland

2 Faculty of Natural Sciences, University of Basel, 4003 Basel, Switzerland

3 Present address: Princeton Neuroscience Institute, Princeton University, 20 Washington Road, 08544 Princeton, New Jersey, USA

Correspondence:
Rainer W. Friedrich
Friedrich Miescher Institute for Biomedical Research, Maulbeerstrasse 66, 4058 Basel, Switzerland
Phone: +41 79 6668072
Email: Rainer.Friedrich@fmi.ch

One of the fundamental questions in neuroscience is how computational functions of neuronal circuits are determined by their connectivity. The olfactory bulb decorrelates and normalizes patterns of sensory input, resulting in a transformation referred to as whitening that supports pattern classification. To analyze the underlying mechanisms we measured odor-evoked activity throughout the OB of a zebrafish larva and reconstructed the wiring diagram in the same specimen by volume electron microscopy. This functional connectomics approach revealed an overrepresentation of triplet connectivity motifs that privilege disynaptic reciprocal inhibition among co-tuned output neurons. This connectivity resulted in strong inhibition of neuronal responses to common features of correlated sensory input patterns. In generic network models, this connectivity was necessary and sufficient to reproduce whitening of naturalistic inputs. These results reveal a specific network topology that is adapted to the statistical structure of olfactory inputs and mediates whitening by feature suppression.

Neuronal activity patterns evoked by natural stimuli contain correlations and intensity variations that reflect the statistics of natural scenes and the tuning of sensory receptors (Simoncelli and Olshausen, 2001). This statistical structure complicates the classification of sensory inputs because it does not usually reflect behaviorally relevant stimulus categories (DiCarlo et al., 2012). For example, visual scenes may be dominated by a large number of pixels representing sky while the biologically most important information is conveyed by a small subset of pixels representing specific objects (e.g., a hawk or a sparrow). Hence, correlations in sensory inputs can complicate meaningful pattern classification and object recognition. This problem can be alleviated by whitening, a fundamental transformation in signal processing that decorrelates patterns and normalizes their variance. Whitening is therefore often used early in a pattern classification process to remove undesired correlations and to optimize the use of coding space (Bishop, 1995).

In the visual and auditory system, whitening of individual neurons' responses to natural stimuli supports efficient coding by redundancy reduction (Atick and Redlich, 1993; Barlow, 1961; Olshausen and Field, 1996; Smith and Lewicki, 2006). Efficient pattern classification, however, requires whitening of activity patterns across neuronal populations. This form of whitening occurs in the olfactory bulb (OB) (Friedrich and Laurent, 2001; Friedrich and Wiechert, 2014; Zhu et al., 2013) where axons of olfactory sensory neurons expressing the same odorant receptor converge onto discrete glomeruli. Odors thus evoke distributed patterns of input activity across array of glomeruli that can overlap substantially when odorants share functional groups (Araneda et al., 2000; Friedrich and Korsching, 1997; Mori et al., 2006). Moreover, the variance (contrast) of glomerular activity patterns varies dramatically as a function of odor concentration. The output of the OB is transmitted to higher brain areas by mitral cells, which receive sensory input from individual glomeruli and interact with other mitral cells via multisynaptic interneuron (IN) pathways (Fig. 1a). Contrary to glomerular inputs, activity patterns across mitral cells become rapidly decorrelated during the initial phase of an odor response (Chu et al., 2016; Friedrich et al., 2004; Friedrich and Laurent, 2001; Gschwend et al., 2015; Niessing and Friedrich, 2010; Yamada et al., 2017)

38 and their variance depends only modestly on stimulus intensity (Banerjee et al., 2015; Zhu et al., 2013).
39 Neuronal circuits in the OB therefore decorrelate and normalize population activity patterns, resulting in
40 whitening of odor representations. However, it remains unclear how this transformation is achieved by
41 interactions between neurons in the OB network.

42 Efficient whitening can be achieved by transformations that are adapted to the correlation structure of
43 input patterns (Simoncelli and Olshausen, 2001). Such adaptive whitening requires prior knowledge about
44 inputs and tuning-dependent connectivity between specific cohorts of neurons. Hence, whitening of
45 sensory representations is thought to depend on an evolutionary memory of stimulus space that is
46 contained in the wiring diagram of neuronal circuits. This hypothesis is difficult to test in the OB because
47 tuning and functional connectivity cannot be inferred from topographical relationships between
48 neurons (Fantana et al., 2008; Friedrich and Korsching, 1997; Soucy et al., 2009; Willhite et al., 2006).
49 Moreover, because interactions between mitral cells are multisynaptic via INs, relevant inhibitory
50 interactions cannot be visualized by transsynaptic tracing across a single synapse.

51 Adaptive whitening and other memory-based processes are likely to depend on higher-order features of
52 neuronal connectivity that cannot be detected by sparse sampling of pairwise connectivity between
53 individual neurons. We therefore used a "functional connectomics" approach that combines population-
54 wide neuronal activity measurements with dense reconstructions of wiring diagrams. To achieve this goal
55 we took advantage of the small size of the larval zebrafish brain. We first measured odor responses of
56 neurons in the OB by multiphoton calcium imaging and subsequently reconstructed the synaptic
57 connectivity among all neurons by serial block-face scanning electron microscopy (SBEM) (Denk et al.,
58 2012; Denk and Horstmann, 2004; Wanner et al., 2016a; Wanner et al., 2016b). We found that higher-
59 order features of multisynaptic connectivity specifically suppress the activity of correlated mitral cell
60 ensembles in a stimulus-dependent manner, resulting in a decorrelation and variance normalization. The
61 wiring diagram of the OB is therefore adapted to the correlation structure of its inputs and mediates a
62 whitening operation based on contrast reduction rather than contrast enhancement.

63

64 **Reconstruction of the wiring diagram and mapping of neuronal activity**

65 We previously acquired an SBEM image stack of the OB in a zebrafish larva and reconstructed 98% of
66 the neurons in the OB (Wanner et al., 2016a; Wanner et al., 2016b). We now annotated the synaptic
67 connections of all OB neurons to reconstruct the full wiring diagram. Human annotators followed each of
68 the reconstructed skeletons and manually labeled all input and output synapses (Fig. 1b,c). Subsequently,
69 synapses of INs were annotated a second time by different annotators. Hence, each synapse involved in
70 MC-IN-MC connectivity motifs should have been encountered at least three times. To obtain a
71 conservative estimate of the wiring diagram with few false positives we retained only those synapses that
72 were annotated at least twice by independent annotators.

73 Each synapse was assigned a unitary weight so that the total connection strength between a pair of
74 neurons equaled the number of synapses. The resulting wiring diagram contained 19,874 MC→IN
75 synapses, 17,524 MC←IN synapses (Fig. 1d), and 13,610 synapses between INs. We also observed
76 contact sites between MCs associated with the same glomerulus where plasma membranes showed strong
77 staining but these sites usually lacked associated vesicles. We did therefore not consider synaptic
78 connections between MCs. On average, connected pairs of MCs and INs made 3.1 MC→IN synapses and
79 2.9 MC←IN synapses per pair. A hallmark of synaptic connectivity in the adult OB are reciprocal
80 dendrodendritic synaptic connections between the same MC-IN pair. In the larval OB, 52% of MC→IN
81 synapses and 51% of MC←IN synapses were associated with a synapse of opposite direction, usually
82 within 2.5 μm, between the same pair of neurons (Fig. 1b, bottom). Hence, reciprocal synaptic
83 connectivity is prominent already in the larval OB of zebrafish.

84 Prior to preparation of the OB sample for SBEM we measured neuronal activity by multiphoton imaging
85 of the calcium indicator GCaMP5, which was expressed under the pan-neuronal elavl3
86 promoter (Akerboom et al., 2013). Somata observed in electron microscopy were mapped onto the light

87 microscopy data using an iterative landmark-based affine alignment procedure followed by manual
88 proofreading (Fig. 2a,b; Supplementary Fig. 1). Somatic calcium signals evoked by four amino acid odors
89 (10^{-4} M) and four bile acid odors (10^{-5} M) were measured sequentially in six optical planes (Fig. 2a;
90 Supplementary Fig. 1) and temporally deconvolved to estimate odor-evoked firing rate changes (Yaksi
91 and Friedrich, 2006). The dynamics of neuronal population activity was then represented by time series of
92 activity vectors for each odor stimulus (232 MCs and 68 INs).

93 Decorrelation and contrast normalization of activity patterns across MCs have been characterized
94 previously in the OB of adult zebrafish (Friedrich et al., 2004; Friedrich and Laurent, 2001; Niessing and
95 Friedrich, 2010) and mice (Chu et al., 2016; Gschwend et al., 2015; Yamada et al., 2017) where >90% of
96 neurons are GABAergic INs. In the larval OB, in contrast, INs account for only 25% of all
97 neurons (Wanner et al., 2016b). Most of these INs are likely to be periglomerular and short axon cells
98 because INs with the typical morphology of granule cells appear only later in development. We therefore
99 asked whether the core circuitry present in the larval OB already performs computations related to
100 whitening.

101 Correlations between activity patterns evoked by different bile acids were high after stimulus onset and
102 decreased during the subsequent few hundred milliseconds (Fig. 2d,e). Patterns evoked by amino acids, in
103 contrast, were less correlated throughout the odor response, which was expected because most amino
104 acids had dissimilar side chains. To quantify pattern decorrelation we focused on activity patterns evoked
105 by bile acids and computed the mean difference in pairwise Pearson correlations between a time window
106 shortly after response onset (t_1) and a later time window (t_2). Time windows were chosen such that the
107 mean population activity across MCs was not significantly different (Fig. 2d; $p = 0.44$, Wilcoxon rank-
108 sum test). Pattern correlations across MCs, however, were significantly lower at t_2 than at t_1 ($p = 0.03$,
109 Wilcoxon rank-sum test), demonstrating that MC activity patterns were reorganized and decorrelated.
110 Activity across INs followed the mean MC activity with a small delay and did not exhibit an obvious
111 decorrelation (Fig. 2d), consistent with observations in the adult OB (Yaksi et al., 2007).

112 The contrast of MC activity patterns, as measured by the variance of activity across the population,
113 increased shortly after stimulus onset and peaked slightly later than the pattern correlation. Subsequently,
114 variance decreased and became more uniform across odors, as reflected by a significant decrease in the
115 standard deviation of the variance across odors between t_2 and t_1 (Fig. 2d; $p < 0.01$, Wilcoxon rank-sum
116 test; t_1 was slightly shifted relative to the time window for correlation analysis to cover the peak of the
117 variance). Hence, MC activity patterns in the larval OB became decorrelated and contrast-normalized,
118 consistent with the whitening of odor representations in the adult OB.

119

120 **Computational consequences of connectivity**

121 While contrast normalization can be achieved by global scaling operations such as divisive
122 normalization (Carandini and Heeger, 2011), pattern decorrelation requires interactions between distinct
123 subsets of neurons (Friedrich and Wiechert, 2014). In theory, pattern decorrelation could be achieved by
124 large networks with sparse and random connectivity (Wiechert et al., 2010) but this architecture is
125 inconsistent with the low number of INs in the larval OB. Smaller networks can decorrelate specific input
126 patterns when their connectivity is specifically adapted to the structure of sensory inputs, suggesting that
127 decorrelation in the OB is an input-specific transformation of odor representations that is encoded in the
128 wiring diagram. In order to explore this hypothesis we first asked whether whitening can be reproduced
129 by implementing the wiring diagram in a network of minimally complex single-neuron models (Fig. 3a).

130 We simulated a network of threshold-linear rate neurons with 208 MCs, representing all recorded MCs
131 with bidirectional connections, and 234 INs, representing all connected INs. Connections between MCs
132 and INs were given by the wiring diagram and excitatory sensory input into MCs was given by the odor-
133 evoked activity pattern at t_1. For simplicity, IN-IN connections were not considered. The time course of
134 stimuli consisted of a fast initial rise followed by a slow decay (Wiechert et al., 2010), approximating the
135 response time course of olfactory sensory neurons in zebrafish (Friedrich and Laurent, 2001). Because

connectivity was fixed, the final network model had only six degrees of freedom (thresholds, synaptic weight scaling factors and time constants of each neuron type).

Correlations between simulated population responses to bile acids increased rapidly and subsequently decreased. Consistent with experimental observations, the mean correlation decreased significantly between two time windows t_1 and t_2 that were chosen so that the mean activity was not significantly different (Fig. 3b,c). The variance (contrast) of activity patterns and its standard deviation across stimuli followed a similar time course but peaked slightly later than the correlation, consistent with experimental observations. Both measures decreased significantly between t_1 and t_2 (Fig. 3b,c; t_1 was adjusted slightly to cover the peak of the variance). Hence, a minimal network implementing the reconstructed connectivity reproduced whitening of biologically realistic inputs. When connectivity was randomized, decorrelation and contrast normalization were both abolished (Fig. 4b-d). We therefore conclude that whitening depends on the wiring diagram.

To further confirm this conclusion we examined whether the reorganization of activity patterns underlying whitening can be predicted from connectivity without an explicit simulation of network dynamics. Activity patterns at t_1 were multiplied with the feed-forward connectivity $W_{MC \rightarrow IN}$ and thresholded to generate a hypothetical pattern of IN activity. This activity pattern was then multiplied with the feed-back connectivity $W_{MC \leftarrow IN}$ to predict the pattern of feedback inhibition, which was subtracted from t_1. This simple algebraic procedure reproduced both pattern decorrelation and variance normalization (Fig. 3c) but failed to do so when connectivity matrices were randomized (not shown), further supporting the conclusion that the wiring diagram contains specific information essential for whitening.

We next performed more specific manipulations to explore how whitening depends on higher-order structure in the wiring diagram. In simulations, we first applied the same permutations to the feed-forward (MC→IN) and feed-back connectivity (MC←IN). This manipulation shuffles the off-diagonal elements in the disynaptic connectivity matrix (lateral inhibition) but preserves the overall distribution of

161 disynaptic MC→IN→MC connection strengths and the on-diagonal elements (self-inhibition; Fig. 3d).
162 Similar to the full randomization of connectivity, this co-permutation abolished whitening (Fig. 3b,c).
163 Moreover, whitening was abolished when input channels were permuted to produce novel input patterns
164 with the same statistical properties and correlations (Fig. 3c). These results show that whitening is
165 mediated by higher-order features of multisynaptic connectivity that are adapted to patterns of sensory
166 input.

167

168 **Mechanisms of whitening**

169 The shortest path between MCs associated with different glomeruli is a disynaptic interaction via one IN
170 (MC-IN-MC). To identify properties of the wiring diagram that mediate whitening we therefore analyzed
171 MC-IN-MC triplets. There are nine possible triplet configurations that represent four topological motifs
172 (Fig. 4a). We found that the motif containing no reciprocal connection (motif 1) was underrepresented
173 whereas the other motifs were overrepresented in comparison to randomized networks (Fig 4b). The
174 strongest overrepresentation was observed for motif 4, which contains reciprocal connections between
175 both MCs and the IN. Hence, MC-IN-MC triplets frequently contained reciprocal connections.

176 To determine whether disynaptic connectivity between MCs depends on their tuning we constructed an
177 input tuning curve for each MC from the responses to the eight odors at t_1. For all pairs of MCs we then
178 quantified the Pearson correlation between their input tuning curves and the number of disynaptic MC-
179 IN-MC connection paths across all motifs. The mean number of disynaptic connections increased with the
180 input tuning correlation (Fig. 4c). Hence, triplets mediate interactions preferentially between MCs with
181 similar tuning.

182 We further analyzed the relationship between triplet motifs and tuning curve similarity. Motifs with
183 reciprocal connections (motifs 2 – 4) were significantly overrepresented among MCs with similar tuning
184 (correlation >0.5; Fig. 4d). This overrepresentation was most pronounced for motif 4 (all connections

185 reciprocal). Hence, disynaptic reciprocal interactions are significantly enriched between MCs with similar
186 tuning.

187 In the retina, unidirectional lateral inhibition between functionally related neurons sharpens tuning curves
188 and enhances pattern contrast (Hartline and Ratliff, 1957) (Fig. 5a, left). In idealized networks with
189 strictly reciprocal connectivity, in contrast, inhibition does not amplify asymmetries in inputs and self-
190 inhibition is usually larger than lateral inhibition (assuming equal synaptic strength; Fig. 5a, right).
191 Hence, reciprocal triplet connectivity among neurons with similar tuning should primarily down-regulate,
192 rather than sharpen, the activity of connected cohorts of neurons. The computational effects of these
193 transformations depend on the properties of input patterns (Supplementary Fig. 2). When inputs follow
194 overlapping Gaussian distributions, contrast enhancement can decorrelate patterns because stimulus-
195 specific information is contained in strong neuronal responses (Barlow, 1961; Hartline and Ratliff, 1957).
196 However, when activity patterns overlap primarily in strongly responsive units, contrast enhancement will
197 fail to decorrelate patterns because it emphasizes non-specific responses. In this scenario, patterns may be
198 decorrelated by the selective inhibition of strongly active cohorts, which may be achieved by specific
199 reciprocal inhibition (Supplementary Fig. 2).

200 To examine the basis of pattern correlations in the OB we analyzed population activity patterns evoked by
201 bile acids at t_1. For each pair of patterns, we quantified the contribution $r_{i,t1}$ of MC i to the Pearson
202 correlation r. Overall pattern correlations were dominated by high contributions from a small fraction of
203 MCs. This subset of MCs was also strongly active, as observed directly when MCs were ranked by their
204 $r_{i,t1}$ (Fig. 5b,c). As a corollary, these MCs also made large contributions to the variance of neuronal
205 activity patterns at t_1 (Fig. 5c). Hence, correlated odor representations overlapped primarily in strongly
206 responsive MCs, consistent with observations in the adult OB (Friedrich and Wiechert, 2014).

207 We then examined the changes in the activity of individual neurons underlying the decorrelation and
208 contrast normalization between t_1 and t_2. The activity of MCs with large $r_{i,t1}$ was significantly lower at t_2
209 than at t_1 (Fig. 5b,c). The activity of MCs that did not strongly contribute to the initial correlation, in

210 contrast, remained similar. As a consequence, the contribution of MCs with large $r_{i,t1}$ to the overall
211 correlation decreased, resulting in a substantial decorrelation of population activity patterns between t_1
212 and t_2. Pattern decorrelation can therefore be attributed, at least in part, to the selective inhibition of MC
213 cohorts that dominate the initial pattern correlations. MCs with high $r_{i,t1}$ also made strong contributions to
214 pattern variance at t_1 (Fig. 5c) because their activity was substantially higher than the population mean.
215 The selective inhibition of these cohorts between t_1 and t_2 changed the activity of these MCs towards the
216 population mean and therefore decreased pattern variance and its s.d. across odors. Pattern decorrelation
217 and contrast normalization can therefore be attributed to a common mechanism that targets inhibition to
218 specific MC cohorts and results in contrast reduction rather than contrast enhancement.

219 The selective suppression of activity in cohorts of co-responsive MCs requires inhibition within cohorts
220 to be stronger than the mean inhibition across the population. To explore how such stimulus- and
221 ensemble-specific inhibition can arise from the connectivity between neurons we selected the 10 MCs
222 with the highest $r_{i,t1}$ for each pair of bile acid stimuli. We then determined the disynaptic MC inputs to
223 these cohorts by retrograde tracing through the wiring diagram across two synapses. Inputs to MCs within
224 a cohort were strongly biased towards MCs of the same cohort (Fig. 5d,e), implying that neurons in a
225 cohort will be strongly inhibited when the cohort is activated as a whole. The specific suppression of
226 activity underlying whitening can therefore be explained by dense reciprocal connectivity within cohorts,
227 which suppresses the representation of stimulus features that activate a cohort.

228 To further explore this hypothesis we continued to analyze the mechanism of whitening in simulations.
229 We first ranked simulated MCs by their $r_{i,t1}$ for bile acid-evoked activity patterns in experiments (same
230 ranking as in Fig. 5c). As observed experimentally, simulated MCs with large $r_{i,t1}$ were strongly inhibited
231 between t_1 and t_2 while the mean activity of other MCs remained unchanged (Fig. 6a). Simulations
232 therefore recapitulated the mechanism of whitening in the OB and precisely predicted the underlying
233 activity changes in individual neurons.

234 We then selected the 10 MCs with the highest $r_{i,t1}$ for each pair of bile acid stimuli (19 MCs in total) and
235 deleted their feedforward connections onto INs in the simulation (11% of all MC→IN connections;
236 Fig. 6b, left). As a control, we deleted the same fraction of feedforward connections between random
237 subsets of neurons. While random deletions had almost no effect, the selective disconnection of functional
238 cohorts abolished pattern decorrelation and variance normalization (Fig. 6c,d). Ranking of MCs by their
239 $r_{i,t1}$ in experimental data demonstrated that the activity of MCs with high $r_{i,t1}$ was reduced slightly
240 between t_1 and t_2 when MC cohorts were selectively disconnected but not as effectively as under control
241 conditions. As a consequence, these MCs continued to make large positive contributions to pattern
242 correlation and variance at t_2 (Fig. 6e). These results show that the selective disconnection of functional
243 cohorts abolished whitening because it disrupted feature suppression. We next randomized all
244 connections except those of the 10 MCs with the highest $r_{i,t1}$ for each bile acid pair (Fig. 6b, right).
245 Results were compared to the full randomization of the wiring diagram, which reduced the inhibition of
246 MC cohorts and abolished whitening (Fig. 3b,c). When connections of functional MC cohorts were
247 selectively preserved, however, the inhibition of MC cohorts remained strong and pattern decorrelation
248 was restored (Fig. 6c,d). Variance normalization was only partially rescued, presumably because
249 preserved cohorts were selected only for their contribution to correlations between bile acid pairs and not
250 for amino acids. The activity of MCs with high $r_{i,t1}$ was strongly reduced (Fig. 6e), demonstrating that
251 pattern decorrelation and partial variance normalization were the result of feature suppression. These
252 results confirm that whitening is mediated by specific disynaptic interactions that suppress the activity of
253 correlation-promoting MC cohorts.

254

255 **Discussion**

256 We used a functional connectomics approach in a small vertebrate to explore the mechanism of whitening
257 in the OB. Whitening is a computation related to object classification and associative memory that
258 requires specific transformations of defined neuronal activity patterns. Such computations are thought to

259 rely on specific wiring diagrams that are adapted to relevant inputs. Consistent with this notion, we found
260 that whitening is achieved by specific multisynaptic interactions that cannot be described by general
261 topographic principles or by the first-order statistics of connectivity between neuron types. Functional
262 connectomics is therefore a promising approach to dissect distributed, memory-based computations
263 underlying higher brain functions.

264 Correlations between input patterns in the OB were dominated by distinct subsets of strongly active input
265 channels. This correlation structure is likely to reflect the co-activation of different odorant receptors by
266 discrete functional groups (Araneda et al., 2000; Mori et al., 2006) and implies that input correlations
267 cannot be removed efficiently by contrast enhancement (Arevian et al., 2008; Cleland and Sethupathy,
268 2006; Yokoi et al., 1995). Rather, patterns are decorrelated by the selective inhibition of strongly active,
269 correlation-promoting MC cohorts. Pattern decorrelation is therefore achieved by contrast reduction,
270 rather than contrast enhancement, which also supports contrast normalization.

271 Whitening requires specific tuning-dependent, disynaptic MC-IN-MC connectivity that may be
272 established by molecular or activity-dependent mechanisms. Because this connectivity exists already
273 before activity-dependent effects were detected on the morphological development of
274 glomeruli (Braubach et al., 2013) the initial assembly of neuronal connections may rely primarily on
275 molecular cues. Projections of INs are enriched between glomeruli that receive input from odorant
276 receptors of the same families (Wanner et al., 2016b), raising the possibility that glomerular targeting of
277 sensory neurons (Nishizumi and Sakano, 2015) and INs involve related mechanisms. However, the
278 development of the connectivity that mediates whitening remain to be explored.

279 Lateral inhibition between neurons with similar tuning is often assumed to sharpen tuning curves by
280 amplifying asymmetries in the input. In the OB, however, triplet connections between related MCs are
281 highly enriched in reciprocal connections. This connectivity results in feedback inhibition that is
282 independent of the precise pattern of MC input to a cohort (Fig. 5a, right) and down-scales the activity of
283 neuronal cohorts without amplifying asymmetries in the input. Reciprocally connected MC↔IN↔MC

284 cohorts therefore mediate feature suppression: in the presence of a feature that effectively activates a
285 cohort, the inhibitory feedback gain within the cohort will be larger than the mean feedback gain and
286 suppress the representation of the feature. This mechanism can explain the selective and odor-dependent
287 inhibition of correlation-promoting MC cohorts.

288 Functional connectomics permitted us to test the significance of this mechanism by implementing the
289 wiring diagram in a network of minimally complex model neurons. Simulations demonstrated that higher-
290 order features of connectivity were necessary and sufficient to produce whitening. Precisely targeted
291 manipulations confirmed that whitening was the result of feature suppression by reciprocal
292 MC↔IN↔MC connectivity among correlation-promoting MC cohorts. Whitening in the OB is therefore
293 produced by a network mechanism that differs from canonical computations in the retina and other
294 sensory systems, presumably because the statistics of sensory inputs differ between sensory modalities.

295 In visual cortex, functionally related principal neurons make stronger excitatory connections than random
296 subsets of neurons (Ko et al., 2011). Such connectivity can arise from Hebbian plasticity mechanisms,
297 enhance representations of sensory features, and amplify specific inputs in memory networks after
298 learning. The disynaptic connectivity observed in the OB, in contrast, results in inhibitory interactions
299 between functionally related principal neurons. Such connectivity cannot be achieved by monosynaptic
300 connectivity between MCs because inhibitory synapses between MCs would violate Dale's law.
301 Functional connectivity in the OB is therefore similar in structure, but opposite in sign, to excitatory
302 connectivity motifs in visual cortex. As a consequence, the connectivity in the OB suppresses, rather than
303 amplifies, specific features in the input. Such a mechanism appears useful to attenuate the impact of
304 irrelevant sensory inputs and to reduce undesired correlations. The mechanism of whitening by feature
305 suppression is consistent with networks that have been optimized for whitening in a theoretical
306 framework with biologically plausible constraints (Pehlevan and Chklovskii, 2015; Zung and Seung,
307 2017). Hence, the mechanism of whitening observed in the OB may represent a general computational
308 strategy in the brain.

References

Akerboom, J., Carreras Calderon, N., Tian, L., Wabnig, S., Prigge, M., Tolo, J., Gordus, A., Orger, M.B., Severi, K.E., Macklin, J.J.*, et al.* (2013). Genetically encoded calcium indicators for multi-color neural activity imaging and combination with optogenetics. Frontiers in molecular neuroscience 6, 2.

Akerboom, J., Chen, T.W., Wardill, T.J., Tian, L., Marvin, J.S., Mutlu, S., Calderon, N.C., Esposti, F., Borghuis, B.G., Sun, X.R.*, et al.* (2012). Optimization of a GCaMP calcium indicator for neural activity imaging. J Neurosci 32, 13819-13840.

Araneda, R.C., Kini, A.D., and Firestein, S. (2000). The molecular receptive range of an odorant receptor. Nature Neurosci 3, 1248-1255.

Arevian, A.C., Kapoor, V., and Urban, N.N. (2008). Activity-dependent gating of lateral inhibition in the mouse olfactory bulb. Nat Neurosci 11, 80-87.

Atick, J.J., and Redlich, A.N. (1993). Convergent algorithm for sensory receptive-field development. Neural Comput 5, 45-60.

Banerjee, A., Marbach, F., Anselmi, F., Koh, M.S., Davis, M.B., Garcia da Silva, P., Delevich, K., Oyibo, H.K., Gupta, P., Li, B., and Albeanu, D.F. (2015). An Interglomerular Circuit Gates Glomerular Output and Implements Gain Control in the Mouse Olfactory Bulb. Neuron 87, 193-207.

Barlow, H.B. (1961). Possible principles underlying the transformations of sensory messages. In Sensory communication, W.A. Rosenblith, ed. (Cambridge, MA: MIT Press), pp. 217-234.

Bishop, C.M. (1995). Neural networks for pattern recognition (Clarendon Press, Oxford).

Braubach, O.R., Miyasaka, N., Koide, T., Yoshihara, Y., Croll, R.P., and Fine, A. (2013). Experience-dependent versus experience-independent postembryonic development of distinct groups of zebrafish olfactory glomeruli. J Neurosci 33, 6905-6916.

Brustein, E., Marandi, N., Kovalchuk, Y., Drapeau, P., and Konnerth, A. (2003). "In vivo" monitoring of neuronal network activity in zebrafish by two-photon Ca^{2+} imaging. Pflügers Arch 446, 766-773.

Carandini, M., and Heeger, D.J. (2011). Normalization as a canonical neural computation. Nat Rev Neurosci 13, 51-62.

Chu, M.W., Li, W.L., and Komiyama, T. (2016). Balancing the Robustness and Efficiency of Odor Representations during Learning. Neuron 92, 174-186.

Cleland, T.A., and Sethupathy, P. (2006). Non-topographical contrast enhancement in the olfactory bulb. BMC Neurosci 7, 7.

Deerinck, T.J., Bushong, E.A., Lev-Ram, V., Shu, X., Tsien, R.Y., and Ellisman, M.H. (2010). Enhancing serial block-face scanning electron microscopy to enable high resolution 3D nanohistology of cells and tissues. Microsc Microanal 16, 1138-1139.

Denk, W., Briggman, K.L., and Helmstaedter, M. (2012). Structural neurobiology: missing link to a mechanistic understanding of neural computation. Nat Rev Neurosci 13, 351-358.

Denk, W., and Horstmann, H. (2004). Serial block-face scanning electron microscopy to reconstruct three-dimensional tissue nanostructure. PLoS Biol 2, e329.

DiCarlo, J.J., Zoccolan, D., and Rust, N.C. (2012). How does the brain solve visual object recognition? Neuron 73, 415-434.

Fantana, A.L., Soucy, E.R., and Meister, M. (2008). Rat olfactory bulb mitral cells receive sparse glomerular inputs. Neuron 59, 802-814.

Friedrich, R.W., Habermann, C.J., and Laurent, G. (2004). Multiplexing using synchrony in the zebrafish olfactory bulb. Nat Neurosci 7, 862-871.

Friedrich, R.W., and Korsching, S.I. (1997). Combinatorial and chemotopic odorant coding in the zebrafish olfactory bulb visualized by optical imaging. Neuron 18, 737-752.

355 Friedrich, R.W., and Laurent, G. (2001). Dynamic optimization of odor representations in the olfactory
356 bulb by slow temporal patterning of mitral cell activity. Science 291, 889-894.
357 Friedrich, R.W., and Wiechert, M.T. (2014). Neuronal circuits and computations: pattern decorrelation in
358 the olfactory bulb. FEBS letters 588, 2504-2513.
359 Gschwend, O., Abraham, N.M., Lagier, S., Begnaud, F., Rodriguez, I., and Carleton, A. (2015). Neuronal
360 pattern separation in the olfactory bulb improves odor discrimination learning. Nat Neurosci 18, 1474-
361 1482.
362 Hartline, H.K., and Ratliff, F. (1957). Inhibitory interaction of receptor units in the eye of *Limulus*. J gen
363 Physiol 40, 357-376.
364 Keller, P.J., Schmidt, A.D., Wittbrodt, J., and Stelzer, E.H. (2011). Digital scanned laser light-sheet
365 fluorescence microscopy (DSLM) of zebrafish and Drosophila embryonic development. Cold Spring
366 Harbor protocols 2011, 1235-1243.
367 Kinkhabwala, A., Riley, M., Koyama, M., Monen, J., Satou, C., Kimura, Y., Higashijima, S., and Fetcho, J.
368 (2011). A structural and functional ground plan for neurons in the hindbrain of zebrafish. Proc Natl Acad
369 Sci U S A 108, 1164-1169.
370 Ko, H., Hofer, S.B., Pichler, B., Buchanan, K.A., Sjostrom, P.J., and Mrsic-Flogel, T.D. (2011). Functional
371 specificity of local synaptic connections in neocortical networks. Nature 473, 87-91.
372 Korogod, N., Petersen, C.C., and Knott, G.W. (2015). Ultrastructural analysis of adult mouse neocortex
373 comparing aldehyde perfusion with cryo fixation. eLife 4, 10.7554/eLife.05793.
374 Li, J., Mack, J.A., Souren, M., Yaksi, E., Higashijima, S., Mione, M., Fetcho, J.R., and Friedrich, R.W. (2005).
375 Early development of functional spatial maps in the zebrafish olfactory bulb. J Neurosci 25, 5784-5795.
376 Mori, K., Takahashi, Y.K., Igarashi, K.M., and Yamaguchi, M. (2006). Maps of odorant molecular features
377 in the mammalian olfactory bulb. Physiol Rev 86, 409-433.
378 Niessing, J., and Friedrich, R.W. (2010). Olfactory pattern classification by discrete neuronal network
379 states. Nature 465, 47-52.
380 Nishizumi, H., and Sakano, H. (2015). Developmental regulation of neural map formation in the mouse
381 olfactory system. Developmental neurobiology 75, 594-607.
382 Olshausen, B.A., and Field, D.J. (1996). Emergence of simple-cell receptive field properties by learning a
383 sparse code for natural images. Nature 381, 607-609.
384 Pehlevan, C., and Chklovskii, D.B. (2015). Optimization theory of Hebbian/anti-Hebbian networks for PCA
385 and whitening. In 2015 53rd Annual Allerton Conference on Communication, Control, and Computing
386 (Allerton) (Monticello, IL), pp. 1458-1465.
387 Pinching, A.J., and Powell, T.P. (1971). The neuropil of the glomeruli of the olfactory bulb. J Cell Sci 9,
388 347-377.
389 Pologruto, T.A., Sabatini, B.L., and Svoboda, K. (2003). ScanImage: flexible software for operating laser
390 scanning microscopes. BioMed Eng OnLine 2, 13.
391 Simoncelli, E.P., and Olshausen, B.A. (2001). Natural image statistics and neural representation. Annu
392 Rev Neurosci 24, 1193-1216.
393 Smith, E.C., and Lewicki, M.S. (2006). Efficient auditory coding. Nature 439, 978-982.
394 Soucy, E.R., Albeanu, D.F., Fantana, A.L., Murthy, V.N., and Meister, M. (2009). Precision and diversity in
395 an odor map on the olfactory bulb. Nat Neurosci 12, 210-220.
396 Suter, B.A., O'Connor, T., Iyer, V., Petreanu, L.T., Hooks, B.M., Kiritani, T., Svoboda, K., and Shepherd,
397 G.M.G. (2010). Ephus: multipurpose data acquisition software for neuroscience experiments. Front
398 Neural Circuits 4, 100.
399 Tabor, R., Yaksi, E., Weislogel, J.M., and Friedrich, R.W. (2004). Processing of odor mixtures in the
400 zebrafish olfactory bulb. J Neurosci 24, 6611-6620.

401 Tapia, J.C., Kasthuri, N., Hayworth, K.J., Schalek, R., Lichtman, J.W., Smith, S.J., and Buchanan, J. (2012).
402 High-contrast en bloc staining of neuronal tissue for field emission scanning electron microscopy. Nat
403 Protoc 7, 193-206.
404 Wanner, A.A., Genoud, C., and Friedrich, R.W. (2016a). 3-dimensional electron microscopic imaging of
405 the zebrafish olfactory bulb and dense reconstruction of neurons. Scientific data 3, 160100.
406 Wanner, A.A., Genoud, C., Masudi, T., Siksou, L., and Friedrich, R.W. (2016b). Dense EM-based
407 reconstruction of the interglomerular projectome in the zebrafish olfactory bulb. Nat Neurosci 19, 816-
408 825.
409 Westerfield, M. (2000). The zebrafish book. A guide for the laboratory use of zebrafish (Danio rerio), 4
410 edn (Eugene, OR: University of Oregon Press).
411 Wiechert, M.T., Judkewitz, B., Riecke, H., and Friedrich, R.W. (2010). Mechanisms of pattern
412 decorrelation by recurrent neuronal circuits. Nature Neurosci 13, 1003-1010.
413 Willhite, D.C., Nguyen, K.T., Masurkar, A.V., Greer, C.A., Shepherd, G.M., and Chen, W.R. (2006). Viral
414 tracing identifies distributed columnar organization in the olfactory bulb. Proc Natl Acad Sci USA 103,
415 12592-12597.
416 Yaksi, E., and Friedrich, R.W. (2006). Reconstruction of firing rate changes across neuronal populations
417 by temporally deconvolved Ca^{2+} imaging. Nature Methods 3, 377-383.
418 Yaksi, E., Judkewitz, B., and Friedrich, R.W. (2007). Topological reorganization of odor representations in
419 the olfactory bulb. PLoS Biol 5, e178.
420 Yamada, Y., Bhaukaurally, K., Madarasz, T.J., Pouget, A., Rodriguez, I., and Carleton, A. (2017). Context-
421 and Output Layer-Dependent Long-Term Ensemble Plasticity in a Sensory Circuit. Neuron 93, 1198-1212
422 e1195.
423 Yokoi, M., Mori, K., and Nakanishi, S. (1995). Refinement of odor molecule tuning by dendrodendritic
424 synaptic inhibition in the olfactory bulb. Proc Natl Acad Sci USA 92, 3371-3375.
425 Zhu, P., Fajardo, O., Shum, J., Zhang Schärer, Y.-P., and Friedrich, R.W. (2012). High-resolution optical
426 control of spatiotemporal neuronal activity patterns in zebrafish using a digital micromirror device. Nat
427 Protoc 7, 1410-1425.
428 Zhu, P., Frank, T., and Friedrich, R.W. (2013). Equalization of odor representations by a network of
429 electrically coupled inhibitory interneurons. Nature Neurosci 16, 1678-1686.
430 Zung, J., and Seung, S. (2017). A correlation game for unsupervised learning yields computational
431 interpretations of Hebbian excitation, anti-Hebbian inhibition, and synapse elimination. arXiv,
432 arXiv:1704.00646v00641

433

434 **Acknowledgements** We thank B. Hu, A. Lüthi, P. Rupprecht and N. Temiz for comments on the
435 manuscript and the Friedrich group for valuable discussions. C. Genoud made outstanding contributions
436 to the acquisition of electron microscopy data. This work was supported by the Novartis Research
437 Foundation, the Human Frontiers Science Program (HFSP), and the Swiss National Science Foundation
438 (SNF).

Author contributions A.A.W. participated in all tasks. He analyzed image data, annotated synapses, supervised human annotators, analyzed data, and wrote the manuscript. R.W.F. analyzed data and wrote the manuscript.

Data availability The data that support the findings of this study are available from the corresponding author upon reasonable request.

445 **Figure Legends**

446

447 **Fig. 1 | Neuronal organization and computations in the OB. a**, Schematic illustration of whitening in
448 the OB. Top: correlated input patterns with different variance. Bottom: decorrelated output patterns with
449 similar variance. Center: Highly simplified illustration of the OB circuit. MCs receive excitatory input
450 from a single glomerulus and interact via inhibitory INs. Whitening requires multisynaptic interactions
451 between specific subsets of MCs that are mediated by INs and defined by the wiring diagram. **b**, Example
452 of a reciprocal synapse between a MC and an IN. **c**, Reconstructions of a MC (left) and an IN (right).
453 Gray volumes show glomeruli, dots depict synapses, colors denote synapse class (unidirectional non-
454 sensory input [blue], unidirectional output [red], reciprocal [magenta], input from sensory neurons
455 [green]). **d**, Simplified representation of the wiring diagram between MCs and INs (binarized connection
456 strength). Colored matrix elements show MC→IN synapses (blue), MC←IN synapses (orange), and
457 reciprocal synapses (black).

458

459 **Fig. 2 | Odor-evoked population activity in the OB. a**, Mapping of the six optical image planes selected
460 for calcium imaging onto the EM-based reconstructions of neurons. Thickness of planes shows range of
461 range of drift between trials. **b**, One optical image plane showing raw GCaMP5 fluorescence (left) and the
462 corresponding oblique slice through the EM image stack (right). Dashed line outlines ipsilateral brain
463 hemisphere; continuous white outlines show glomerular neuropil. Tel, telencephalon; OB, olfactory bulb.
464 Region outlined by the red square is enlarged; white dots depict somata in corresponding locations.
465 Bottom left: fluorescence change evoked by an odor stimulus in the same field of view. Arrowheads
466 depict locations of two responsive somata in different images. **c**, Activity of MCs (n = 232) and INs
467 (n = 68) in response to four bile acids (BAs) and four amino acids (AAs) during two time windows, t_1 and
468 t_2. **d**, Left: time courses of odor-evoked activity, pattern correlation (Pearson) and pattern variance.
469 Horizontal bar indicates time of odor stimulation. Black: mean measures across MCs. Gray: individual
470 odors (variance) or odor pairs (correlation). Light blue: mean measures across INs. Correlation was
471 measured only between activity patterns evoked by bile acids because patterns evoked by amino acids
472 were dissimilar already at response onset. Right: Mean measures for MCs during t_1 and t_2. **e**, Matrices
473 showing Pearson correlations between activity patterns across MCs (left) and INs (right) at t_1 and t_2.
474 Odors: TCA, taurocholic acid; GCA, glycocholic acid; GCDCA, glycochenodeoxycholic acid; TDCA,
475 taurodeoxycholic acid; Trp, tryptophan; Phe, phenylalanine; Val, valine; Lys, lysine.

476

Fig. 3 | Whitening depends on connectivity. a, Architecture of simulated network with connections between MCs and INs. **b**, Time courses of simulated odor-evoked activity, pattern correlation and pattern variance obtained with different wiring diagrams. Blue: original wiring diagram obtained by circuit reconstruction. Dark red: fully randomized connectivity. Light red: co-permutation of feed-forward (MC→IN) and feed-back (MC←IN) connectivity. Shaded areas show s.d. across different permutations. **c**, Mean pattern correlation and s.d. of pattern variance at t_2. S.d. of pattern variance is normalized to the value observed experimentally at t_1. Horizontal black lines show mean experimental values at t_1. Statistical comparisons of correlation and s.d. of variance were performed using a Mann-Whitney U test and an F-test, respectively. For experimental results and simulations using the reconstructed wiring diagram error bars show s.d. across odor pairs (correlation; bile acids only) or individual odors (s.d. of variance). Significance tests compare values at t_2 to experimental values at t_1. For other simulation results, error bars show s.d. over 20 repetitions. Significance tests compare the mean over repetitions to the mean observed experimentally at t_1. *, $p < 0.05$; **, $p < 0.01$; ***, $p < 0.001$; n.s., not significant. **d**, Top: disynaptic connectivity matrix between MCs ($W_{MC\rightarrow IN} * W_{MC\leftarrow IN}$). Grayscale represents number of disynaptic MC-IN-MC connections (normalized). Bottom: example of a disynaptic connectivity matrix with the same order of MCs after co-permuting $W_{MC\rightarrow IN}$ and $W_{MC\leftarrow IN}$.

Fig. 4 | Tuning-dependent disynaptic connectivity in the OB. a, Classes of triplet connectivity motifs between MCs and INs. **b**, Left: number of connectivity motifs found in the wiring diagram (considering only MCs with activity measurements; n = 232). Right: z-score quantifying over- or under-representation of motifs as compared to 10,000 independent randomizations. **c**, Number of disynaptic connections between MCs as a function of tuning similarity (signal correlation; binned; mean ± s.e.m.). Black: all MCs (n = 21,528 pairs); gray: excluding MCs without at least one strong odor response (n = 7,875 pairs). **d**, Over- and under-representation of connectivity motifs among MC pairs with high signal correlation ($r_{Signal} > 0.5$; black) and among the remaining pairs ($r_{Signal} \leq 0.5$; gray).

Fig. 5 | Disynaptic connectivity underlying feature suppression. a, Schematic illustration of contrast enhancement by unidirectional lateral inhibition (left) and down-scaling of cohort activity by reciprocal inhibition (right; feature suppression). Arrow length and grayscale indicate activity. **b**, Example of MC activity patterns evoked by two bile acids (TCA, GCDCA) that were decorrelated between t_1 and t_2. MCs are ranked from top to bottom by their individual contribution to the pattern correlation r at t_1 ($r_{i,t1}$). **c**, Left: average contribution of MCs to all pairwise correlations between activity patterns evoked by bile

acids at t_1 and t_2. MCs were ranked by $r_{i,t1}$ for each pair of patterns as in **b**. Sorted vectors of correlation contributions were then averaged over odor pairs. Center, right: Mean bile-acid evoked activity of MCs and mean contribution of MCs to pattern variance. MCs were sorted by $r_{i,t1}$ and averaged as in the left panel. Gray and black curves show correlation contribution, activity, and variance contribution at t_1 and t_2, respectively (same sorting of individual neurons by $r_{i,t1}$ for all curves). Insets enlarge the top part of the curves (20 MCs with highest $r_{i,t1}$). **d**, Example of disynaptic retrograde tracing of functional cohorts in the wiring diagram. Blue: three MCs with highest $r_{i,t1}$ for the odor pair shown in **b** ("starter MCs"). Green: 12 INs with largest number of synaptic inputs to the starter MCs. Red: 48 MCs with largest number of disynaptic inputs to the starter MCs. Transparency represents the number of synaptic connections. Note that the MCs with strong disynaptic connectivity to the starter MCs include the starter MCs themselves, consistent with pronounced reciprocal connectivity among functionally related MC cohorts. **e**, Disynaptic MC-IN-MC connectivity as a function of correlation contribution at t_1 ($r_{i,t1}$; same ranking as in **b** and **c**). For each pair of bile acids, the 10 MCs with the highest $r_{i,t1}$ were selected as starter cells. Disynaptic inputs from all MCs were then represented in a vector and averaged over odor pairs. Note strong overrepresentation of disynaptic connectivity within the cohort of starter cells (gray shading).

Fig. 6 | Mechanism of whitening analyzed by targeted manipulations of the wiring diagram. a, Mean correlation contribution, activity, and variance contribution of MCs responding to bile acids at t_1 (light blue) and t_2 (dark blue) in simulations. MCs were ranked by the correlation contribution $r_{i,t1}$ observed in experimental data as in **Fig. 5c**. Insets enlarge the top parts of the curves (20 MCs with highest $r_{i,t1}$) and compare simulation results to experimental data (gray, black) for the same 20 MCs. **b**, Schematic: selective deletion and selective preservation MC cohort connectivity in simulations. **c**, Mean pattern correlation and s.d. of pattern variance (normalized) at t_2 observed in simulations under different conditions. S.d. of pattern variance has been normalized to the experimentally observed value at t_1. Horizontal black lines show mean values at t_1; vertical bars show change relative to t_1. Statistical comparisons of correlation and s.d. of variance were performed using a Mann-Whitney test and an F-test, respectively. Error bars for original wiring diagram show s.d. across odor pairs (correlation; bile acids only) or individual odors (s.d. of variance); significance tests compare values at t_2 to experimental values at t_1. Other error bars show s.d. over means from 20 simulations and significance tests compare the mean over repetitions to the mean observed experimentally at t_1. **, $p < 0.01$; ***, $p < 0.001$; 0.05, $p = 0.05$; n.s., not significant. **d**, Time courses of pattern correlation and of the s.d. of pattern variance in simulations using different wiring diagrams. Shaded area shows s.d. across different permutations. **e**, Mean correlation contribution, activity, and variance contribution of the 20 MCs with the highest $r_{i,t1}$

observed experimentally and in simulations using different wiring diagrams. MCs were ranked by $r_{i,t1}$ observed in experimental data as in **a** and in **Fig. 5c** (same ranking under all conditions). Gray: t_1; Colored: t_2. Shading shows s.d. across 20 different permutations. Note that the reduction in correlation contribution, activity and variance contribution among MCs with high $r_{i,t1}$ is decreased when connectivity is modified globally or in functional cohorts, but not when connectivity of functional cohorts is preserved.

Supplementary Fig. 1 | Mapping of datasets and activity measurements. a, Displacement of regions of interest (ROIs) during manual proofreading. ROIs representing somata were mapped from the EM dataset to optical image planes in each trial by an affine transformation that was determined by an iterative landmark-based procedure (Methods). Subsequently, the position of each ROI was adjusted manually on the optical image (n = 7,280 ROIs; six image planes with 11 trials each). The mean displacement (± s.d.) during manual adjustment (proofreading) was small (593 ± 833 nm), implying that automated mapping was highly reliable. **b**, Raw calcium signals (ΔF/F) evoked by eight odors in neurons that were present in all trials (208 MCs and 68 INs). Gray bars indicate odor stimulation.

Supplementary Fig. 2 | Effects of pattern transformations on pattern correlation. a, Effect of contrast enhancement on the correlation between displaced Gaussian patterns. In such patterns, strongly active units convey stimulus-specific information while weakly active units tend to be non-specific. Contrast enhancement therefore decorrelates patterns because it emphasizes strongly active units and suppresses weakly active units. **b**, Effect of contrast enhancement on the correlation between activity pattern that overlap in strongly active units. Contrast enhancement fails to decorrelate patterns because pattern-specific information is conveyed by moderately or weakly active units. **c**, Patterns that overlap in strongly active units are decorrelated by selective inhibition of strongly active units, which results in contrast reduction. Patterns are decorrelated because the relative contribution of moderately or weakly active units is enhanced. Selective inhibition of strongly active units is generated by dense reciprocal inhibition within cohorts of co-tuned neurons. Inhibitory feedback gain is therefore higher than the average inhibitory feedback gain within a co-tuned cohort when the stimulus feature that activates the cohort is present (feature suppression).

570 **Methods**

571 **Animals and preparation**. Adult zebrafish (Danio rerio) were maintained and bred under standard
572 conditions at 26.5°C. Embryos and larvae of a double-transgenic line
573 (elavl3:GCaMP5 x vglut:DsRed) (Akerboom et al., 2012; Kinkhabwala et al., 2011) in nacre
574 background were raised at 28.5°C in standard E3 medium (Westerfield, 2000).

575 Imaging experiments were performed as described previously (Li et al., 2005). In brief, larvae 4 - 5 days
576 post fertilization (dpf) were contained in a small drop of aerated E3 without methylene blue or N-
577 phenylthiourea. Larvae were then paralyzed by addition of 20 µl of fresh mivacurium chloride (Mivacron,
578 GlaxoSmithKline, Munich, Germany) (Brustein et al., 2003) and embedded in 2% low-melting agarose
579 (type VII; Sigma, St Louis, MO, USA) in a perfusion chamber that was inclined by 30° to improve dorsal
580 optical access to the OBs. Agarose covering the noses was carefully removed. A constant stream of E3
581 (2 ml/min) was delivered through a tube in front of the nose and removed by continuous suction.
582 Throughout the experiment it was ensured that larvae showed normal heartbeat. Larvae that were not
583 fixed for EM recovered from paralysis after a few hours and continued to develop without obvious
584 defects. All animal procedures were performed in accordance with official animal care guidelines and
585 approved by the Veterinary Department of the Canton of Basel-Stadt (Switzerland).

586 **Odor stimulation**. Odor application was performed as described (Li et al., 2005). In brief, odors were
587 delivered to the nose through the E3 medium using a computer-controlled, pneumatically actuated HPLC
588 injection valve (Rheodyne, Rohnert Park, CA, USA). All experiments were carried out at room
589 temperature (~22°C). The odor set comprised one food odor (Tabor et al., 2004), four bile acids
590 (glycochenodeoxycholic acid [GCDCA], taurocholic acid [TCA], taurodeoxycholic acid [TDCA] and
591 glycocholic acid [GCA]; Sigma Aldrich, Munich, Germany) and four amino acids (Trp, Lys, Phe, and
592 Val; Fluka, Neu-Ulm, Germany). Stock solutions of GCDCA, TCA, TDCA, Trp, Lys, Phe and Val at
593 5×10^{-3} M in E3 were kept refrigerated and diluted 1:500 (GCDCA, TCA, TDCA) or 1 : 50 (Trp, Lys,
594 Phe, Val) in aerated E3 medium immediately before the experiment. A stock solution of GCA was

595 prepared in 50% ethanol/50% E3 at 2.5×10^{-3} M, refrigerated, and diluted 1:250 immediately before the
596 experiment. In a given trial, an odor was applied twice for a duration of ~3 s with an inter-stimulus
597 interval of 60 s. Successive trials with different odors were separated by at least 2 min.

598 **Multiphoton calcium imaging**. Multiphoton imaging was performed using a microscope equipped with a
599 mode-locked Ti:sapphire laser (SpectraPhysics) and a 20× objective (NA 1.0, Zeiss) as described (Zhu et
600 al., 2012). GCaMP5 was excited at 910 nm and emission was detected through green (535 ± 25 nm) and
601 red (610 ± 37.5 nm) emission filters in separate channels. Images (256 × 256 pixels) were acquired at
602 128 ms per frame using SCANIMAGE and EPHUS software (Pologruto et al., 2003; Suter et al., 2010)
603 for a total of 2 min in each trial. Trials were performed sequentially in six focal planes that were separated
604 by approximately 10 µm along the dorso-ventral axis of the OB. The field of view covered the entire
605 cross-section of the OB and parts of the adjacent telencephalon. Ten stimulus trials (nine odors and one
606 E3 control), each including two odor applications, were performed in each focal plane. The order of
607 stimuli was E3, food, GCDCA, TCA, TDCA, GCA, Trp, Lys, Phe, Val. In addition, 2 min of spontaneous
608 activity were recorded in each focal plane. After completion of all trials a stack of images covering the
609 whole olfactory bulb was acquired with a z-step interval of 0.5 µm.

610 **Automated drift correction**. Slow mechanical drift, which may be caused by capillary forces acting on
611 the agarose matrix (Keller et al., 2011), was corrected for by an automated routine. This routine acquired
612 a small stack (± 3 µm around the focus; 0.5 µm steps) and compared images to a reference by cross-
613 correlation after standardizing image columns and rows. The field of view was then automatically
614 translated in X,Y and Z to maximize the cross-correlation to the reference.

615 **Electron microscopy**. Preparation and imaging of this sample have been described previously (Wanner et
616 al. 2016a, Wanner et al. 2016b). Briefly, tissue was stained *en bloc* with osmium, uranyl acetate and lead
617 aspartate using an established protocol (Deerinck et al., 2010; Tapia et al., 2012) with minor
618 modifications and embedded in Epon resin with silver particles to minimize charging (Wanner et al.,
619 2016a; Wanner et al., 2016b). Multi-tile images were acquired in high vacuum using a scanning electron

620 microscope (QuantaFEG 200; FEI) equipped with an automated ultramicrotome inside the vacuum
621 chamber (3View; Gatan). Section thickness was 25 nm, pixel size was 9.25×9.25 nm^2, and the electron
622 dose was 17.5 $e^- nm^{-2}$. The dataset comprised 4,746 successive sections of which one section was lost due
623 to technical problems. The final stack was cropped to a size of $72.2 \times 107.8 \times 118.6$ µm^3.

624 **Neuron reconstruction and synapse annotation**. Skeletons of all neurons in the OB were reconstructed
625 previously as described (Wanner et al., 2016a; Wanner et al., 2016b). Briefly, three independent skeletons
626 of each neuron were generated manually from seed points at somata. Skeletons were converged and
627 mismatches were corrected as described, and high accuracy was verified by measures of precision and
628 recall (Wanner et al., 2016b). Tracing was performed using KNOSSOS (www.knossostool.org) or
629 PyKNOSSOS (https://github.com/adwanner/PyKNOSSOS). Most skeletons were generated by a
630 professional high-throughput image annotation service (www.ariadne.ai).

631 Synapses were annotated manually using PyKNOSSOS in "flight" mode (Wanner et al., 2016a). In the
632 default configuration, PyKNOSSOS displays image data in four viewports: the YX viewport (imaging
633 plane) and three mutually orthogonal viewports of arbitrary orientation. In "flight" mode, the latter is
634 perpendicular to the direction of the current neurite. We found that this "auto-orthogonal" view increases
635 tracing speed and facilitates the identification of branch points and synapses. Annotators followed
636 skeletonized reference neurons along pre-calculated paths to ensure that all neurites were annotated. Most
637 synapses were annotated by a professional image annotation service (www.ariadne.ai).

638 Synapses were identified by a cloud of vesicles that touched the plasma membrane, often at a site of
639 intense staining. Annotators defined synapses by placing three nodes: (1) a node in the presynapse, (2) a
640 node in the synaptic cleft, and (3) a node in the postsynapse. Nodes in the presynapse and postsynapse are
641 skeleton nodes of the pre- and postsynaptic neurons if these skeletons are available. In addition,
642 annotators assigned a confidence level c to each synapse. This confidence level was introduced because
643 synapse identification is not unambiguous; rather, human experts can disagree whether a given structure
644 is a synapse or not even when image quality is high.

645 Synapses were then classified as either “input synapse”, “output synapse”, “sensory synapse” or
646 “unknown”. Input and output synapses are synapses of the reference neuron with the corresponding
647 directions, excluding synapses with sensory neurons. Sensory synapses are input synapses received by the
648 reference neuron from axons of sensory neurons, which were identified by their dark cytoplasm (Pinching
649 and Powell, 1971). Unknown structures resemble synapses but do not display all characteristic features.
650 These structures often included an intense staining of the membrane but no clearly associated vesicle
651 cloud. We therefore speculate that some of these structures may be gap junctions.

652 We first annotated input and output synapses of all MCs and INs independently of each other. Hence,
653 each synapse should have been encountered twice, once from the presynaptic and once from the
654 postsynaptic side. Synapses of INs were then annotated again by different individuals, resulting in a 3-
655 fold redundancy for each MC-IN synapse. In order to minimize the number of false positives the final
656 wiring diagram retained only those MC-IN synapses that were annotated on the MC and at least once on
657 the IN.

658 Each synapse was assigned a unitary weight. As a consequence, the strength of the connection between
659 two neurons in each direction was given by the number of synapses between this pair of neurons. In
660 addition, we tested two other methods to determine synaptic strength. First, connection strength was
661 binarized such that all connections had strengths 0 or 1, independent of the number of synapses. Second,
662 we defined the weight of a synapse as its mean confidence level c, and the total weight of a connection as
663 the sum of the confidence levels of all synapses. In addition, we tested various confidence thresholds to
664 discard synapses with low confidence before determining the weights. Similar results were obtained with
665 all methods and a wide range of confidence thresholds, implying that results are highly robust.

666 **Correlation between multiphoton and SBEM image stacks**. Mapping of multiphoton to SBEM image
667 data may be complicated by (1) mechanical distortions introduced by the sample preparation procedure,
668 (2) shrinkage due to loss of extracellular space induced by chemical fixation (Korogod et al., 2015), and
669 (3) developmental changes occurring during the approximately three hours between the first calcium

670 imaging trial and the final fixation of the tissue. Initial observations indicated that distortions between
671 image datasets were mostly linear (rotation, translation, shrinkage) while non-linear distortions appeared
672 minimal and developmental changes were negligible. We therefore used an affine transformation to map
673 multiphoton images into the SBEM stack, followed by manual fine adjustment of regions of interest
674 (ROIs) for the extraction of calcium signals.

675 An initial affine transformation matrix was fitted to a set of corresponding points that were selected
676 manually in both datasets. The EM volume was then transformed onto the two-photon images, the
677 position of existing points were optimized manually, and additional pairs of corresponding points were
678 selected. The transform was then re-calculated based on the updated set of landmarks and this procedure
679 was iterated until asymptotic behavior was observed.

680 All somata of the OB were outlined manually in the SBEM dataset and mapped onto the time-averaged
681 multiphoton fluorescence images of each trial, resulting in 7280 mappings of somatic outlines in the
682 SBEM dataset to regions of interest (ROIs) in 66 multiphoton images (11 trials at each of six optical
683 planes). The position of all ROIs was then manually adjusted to optimize the mapping in each trial. The
684 average displacement of ROIs during manual adjustment was small (593 ± 833 nm; mean ± s.d.;
685 Supplementary Fig. 1), demonstrating that the accuracy of the initial affine mapping was already high.

686 **Analysis of calcium signals**. Individual frames of multiphoton image time series were low-pass spatially
687 filtered with a mild 2D Gaussian kernel ($\sigma = 1.2$ pixels). Baseline fluorescence F was calculated as the
688 average fluorescence during a 2 s window before response onset. Traces representing relative changes in
689 fluorescence ($\Delta F/F$) in each ROI were averaged over the two successive odor applications in each trial
690 and band-pass filtered in time using a Butterworth filter with a cutoff frequency of 0.2 times the frame
691 rate. The average population response onset ($t = 0$) was determined manually from all raw $\Delta F/F$ traces
692 and fixed for all trials. Firing rate changes of neurons represented by individual ROIs were estimated by
693 temporal deconvolution of calcium signals as described (Yaksi and Friedrich, 2006) using standard
694 parameters ($\tau_{decay} = 3$ s, $thr_{noise} = 0$).

695 Analyses of population activity were restricted to neurons represented by ROIs with a radius ≥2 pixels in
696 all trials (corresponding to an area of 3.14 μm^2; 232 MCs and 68 INs). For network simulations and
697 mechanistic analyses of whitening we considered only the 208 MCs that were pre- and post-synaptic to at
698 least one IN and excluded 24 presumably premature MCs. Population responses to different odors were
699 compared by calculating the Pearson correlation coefficient between the population activity vectors of
700 MCs for the different stimuli at a given time point after response onset.

701 **Network modeling**. Excitatory MCs and inhibitory INs were simulated as threshold-linear units with a
702 state variable representing firing rate. The $r^i(t)$ and $u^j(t)$ representing firing rates of MC *i* and IN *j*,
703 respectively, followed the equations of motion

704 $$\tau_{MC}^{i} \cdot \frac{dr^i(t)}{dt} = -r^i(t) + G_{sen}^{i} S^i(t) - G_{inh}^{i} W_{MC \leftarrow IN} \cdot [u(t) - \theta_{IN}]_+$$

705 $$\tau_{IN}^{j} \cdot \frac{du^j(t)}{dt} = -u^j(t) + G_{exc}^{j} W_{IN \leftarrow MC} \cdot [r(t) - \theta_{MC}]_+$$

706 where the vectors r θ_{MC} and θ_{IN} are firing thresholds, $W_{MC \leftarrow IN}$ and $W_{IN \leftarrow MC}$ correspond to the
707 reconstructed IN-to-MC and MC-to-IN connectivity weight matrices, respectively, and the vectors $r(t)$
708 and $u(t)$ represent the firing rates of the MC and IN, respectively. $[]_+$ denotes half-wave rectification:

709 $$[x(t)]_+ = \begin{cases} 0, & x(t) < 0 \\ x(t), & x(t) \geq 0 \end{cases}$$

710 τ_{MC}^{i} and τ_{IN}^{j} are the time constants for the individual MCs and INs, respectively. G_{sen}^{i}, G_{inh}^{i} and G_{exc}^{j} are
711 the individual scaling factor for sensory, inhibitory and excitatory input, respectively. To account for the
712 natural variability in biological systems, the parameter values for each of the cells in each of the
713 individual simulation runs were drawn from a Gaussian distribution with a standard deviation of 1% of
714 the distribution mean. The distribution means of the different parameters were:

715 G_{sen} = 2.5, G_{exc} = 3.25, G_{inh} = 5.5, θ_{MC} = 3.6, θ_{IN} = 110, τ_{MC} = 1, τ_{IN} = 250;

716 The time course of sensory input $S^i(t)$ was modelled as difference of exponentials as described

717 previously (Wiechert et al., 2010):

718 $\tilde{s}(t) = -a_{j,\infty} + \frac{a_{j,\infty}}{1-\alpha}(1 - e^{-\tau_r t} - \alpha + \alpha e^{-\tau_d t})$ with $\alpha = 0.8, \tau_r = {}^{1}/_{150}, \tau_d = {}^{1}/_{600}, a_{j,\infty} = {}^{1}/_{150}$

719 To model $S_i(t)$, the individual sensory input of MC *i*, we used its experimentally measured activity

720 $\hat{a}_i$ during t_1 and modulated the time course according to $\tilde{s}(t)$:

721 $S_i(t) = \hat{a}_i \frac{\tilde{s}(t)}{\tilde{s}_{max}}$, where $\tilde{s}_{max} = \max_{t \geq 0}(\tilde{s}(t))$

722 The differential equations were solved in MATLAB with a fixed step size of 1 millisecond using a first

723 degree Newton-Cotes integration scheme or using an adaptive step size embedded Runge-Kutta-Fehlberg

724 (4, 5) scheme. Both integration schemes lead to qualitatively very similar results, and therefore the former

725 method was used for simplicity for the simulated data shown here.

726 In an iterative, semi-automated parameter search, we identified a suitable parameter range that fulfilled

727 the following criteria:

728 (1) The peak firing rates of individual neurons does not exceed a physiologically realistic range (< 200

729 Hz).

730 (2) The strength of inhibition is appropriate to reproduce the time course of the average population

731 activity, correlation and variance.

732 (3) The activity, correlation contribution and variance contribution of individual MCs at t_1 and t_2 is in

733 good correspondence to experimental measurements.

734 Parameters for which these criteria were fulfilled were found by parameter variations in pilot studies.

735 Results were usually robust against variations of each parameter by ±50% around the values reported

736 above.

Analysis of triplet motifs. Occurrences of disynaptic MC-IN-MC motifs were counted after binarizing connections. We enumerated all neuron triplet combinations in the reconstructed wiring diagram and tested for graph isomorphism against all 4 disynaptic motif types. The obtained motif counts were compared against a reference model where the forward and backward connectivity of the MCs were permuted independently while maintaining the node count and edge density (n = 10 000 permutations). The z-scores and p-values were obtained by computing the mean and standard deviation of each motif type in the permuted networks.

To compare the motif frequency as a function of the pairwise tuning similarity, we divided the MC pairs into two groups, one with similar tuning ($r_{signal} > 0.5$) and one with dissimilar tuning ($r_{signal} \leq 0.5$) and counted the occurrences of MC-IN-MC motifs in each group. We then compared the motif counts against a reference model where we permuted the pairwise tuning similarity between MCs and regrouped them by tuning similarity ($r_{signal} > 0.5$ versus $r_{signal} \leq 0.5$) while maintaining the same network topology (n = 10 000 permutations). The z-scores and p-values were then obtained by computing the mean and standard deviation of each motif type in the permuted groups (Fig 4d).

Additional analyses. The contribution of individual MCs to the Pearson correlation coefficient

$$r = \frac{1}{n-1}\sum_{i=1}^{n}\left(\frac{x_i - \bar{x}}{sd_x}\right)\left(\frac{y_i - \bar{y}}{sd_y}\right)$$

between population activity patterns was calculated by determining the summand $\left(\frac{x_i - \bar{x}}{sd_x}\right)\left(\frac{y_i - \bar{y}}{sd_y}\right)$ for each MC. Similarly, the contribution of individual MCs to the variance

$$sd_x^2 = \frac{1}{n-1}\sum_{i=1}^{n}(x_i - \bar{x})^2$$

of the population activity patterns was calculated by determining the summand $(x_i - \bar{x})^2$ for each MC. Here, x_i and y_i are responses of MCs to odors x and y, sd_x and sd_y are the standard deviations of population responses to odors x and y, and n is the total number of MCs in the population.

Statistical significance was tested using a non-parametric Mann-Whitney U test unless noted otherwise.

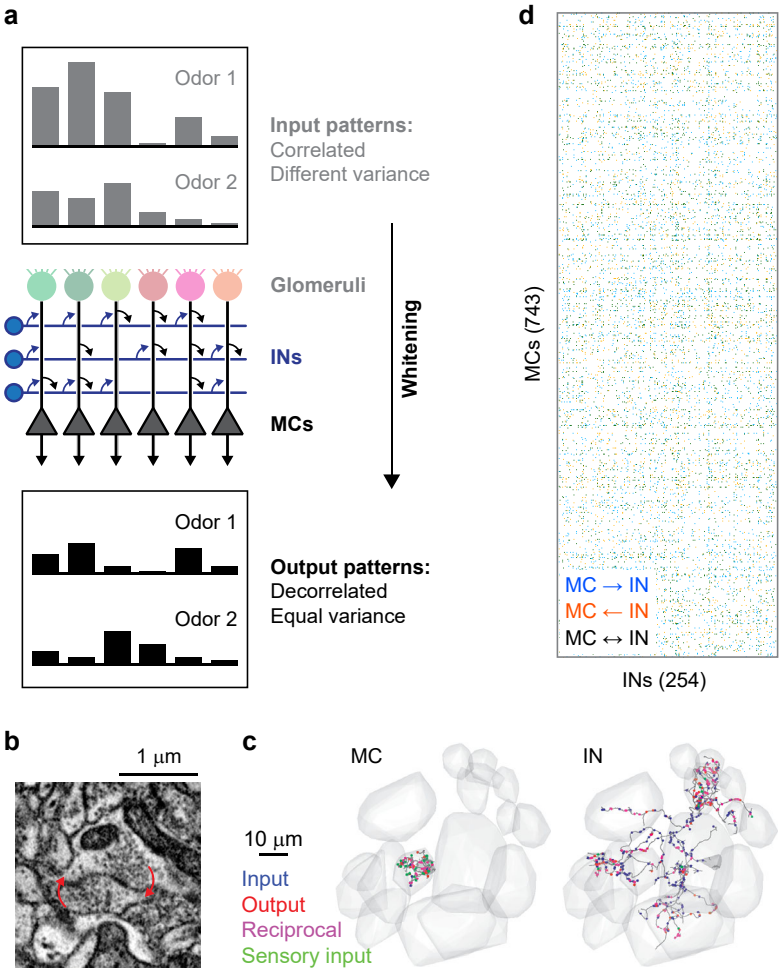

Fig. 1 | Neuronal organization and computations in the OB. a, Schematic illustration of whitening in the OB. Top: correlated input patterns with different variance. Bottom: decorrelated output patterns with similar variance. Center: Highly simplified illustration of the OB circuit. MCs receive excitatory input from a single glomerulus and interact via inhibitory INs. Whitening requires multisynaptic interactions between specific subsets of MCs that are mediated by INs and defined by the wiring diagram. **b**, Example of a reciprocal synapse between a MC and an IN. **c**, Reconstructions of a MC (left) and an IN (right). Gray volumes show glomeruli, dots depict synapses, colors denote synapse class (unidirectional non-sensory input [blue], unidirectional output [red], reciprocal [magenta], input from sensory neurons [green]). **d**, Simplified representation of the wiring diagram between MCs and INs (binarized connection strength). Colored matrix elements show MC→IN synapses (blue), MC←IN synapses (orange), and reciprocal synapses (black).

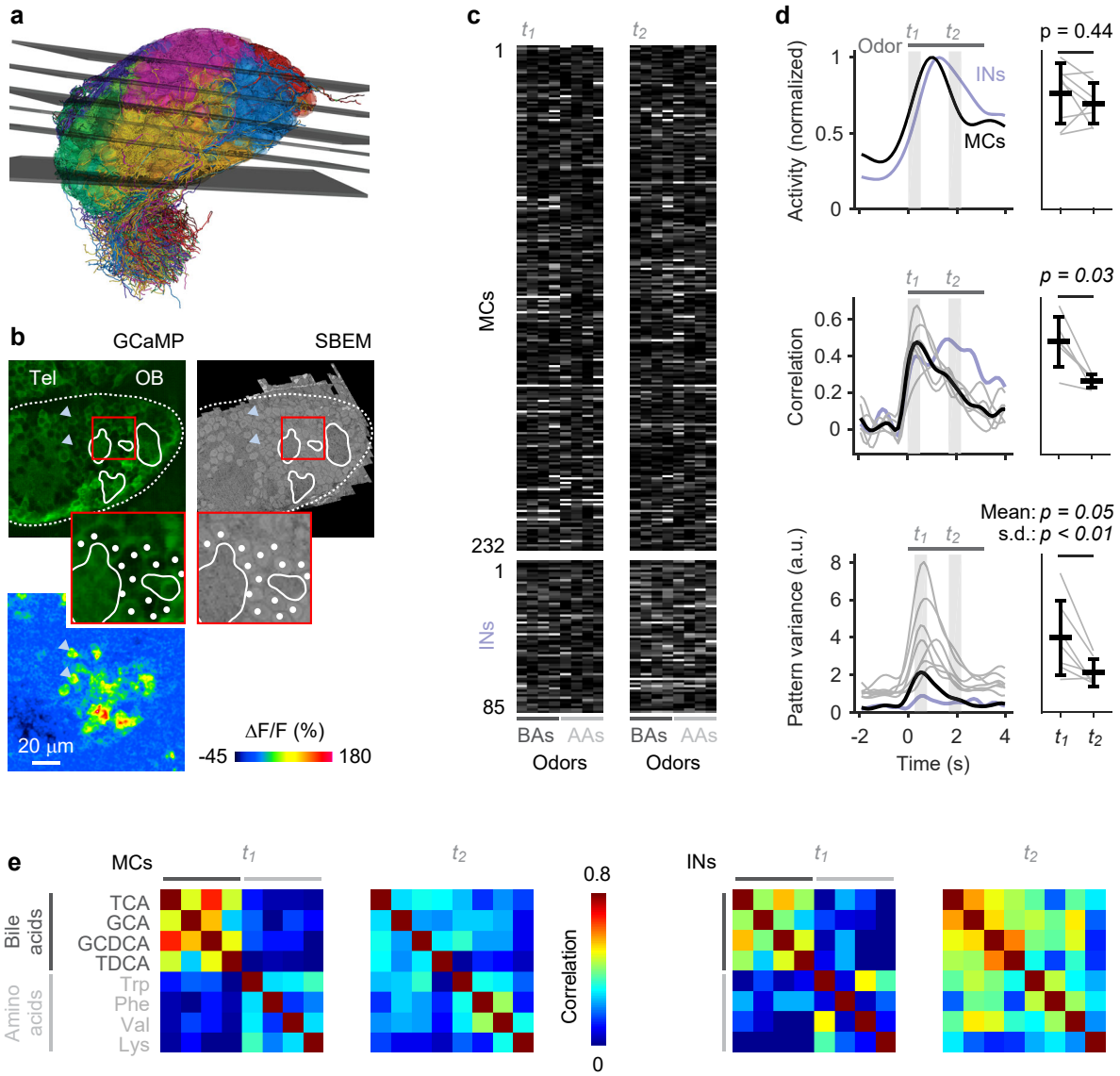

Fig. 2 | Odor-evoked population activity in the OB. a, Mapping of the six optical image planes selected for calcium imaging onto the EM-based reconstructions of neurons. Thickness of planes shows range of range of drift between trials. **b**, One optical image plane showing raw GCaMP5 fluorescence (left) and the corresponding oblique slice through the EM image stack (right). Dashed line outlines ipsilateral brain hemisphere; continuous white outlines show glomerular neuropil. Tel, telencephalon; OB, olfactory bulb. Region outlined by the red square is enlarged; white dots depict somata in corresponding locations. Bottom left: fluorescence change evoked by an odor stimulus in the same field of view. Arrowheads depict locations of two responsive somata in different images. **c**, Activity of MCs (n = 232) and INs (n = 68) in response to four bile acids (BAs) and four amino acids (AAs) during two time windows, t_1 and t_2. **d**, Left: time courses of odor-evoked activity, pattern correlation (Pearson) and pattern variance. Horizontal bar indicates time of odor stimulation. Black: mean measures across MCs. Gray: individual odors (variance) or odor pairs (correlation). Light blue: mean measures across INs. Correlation was measured only between activity patterns evoked by bile acids because patterns evoked by amino acids were dissimilar already at response onset. Right: Mean measures for MCs during t_1 and t_2. **e**, Matrices showing Pearson correlations between activity patterns across MCs (left) and INs (right) at t_1 and t_2. Odors: TCA, taurocholic acid; GCA, glycocholic acid; GCDCA, glycochenodeoxycholic acid; TDCA, taurodeoxycholic acid; Trp, tryptophan; Phe, phenylalanine; Val, valine; Lys, lysine.

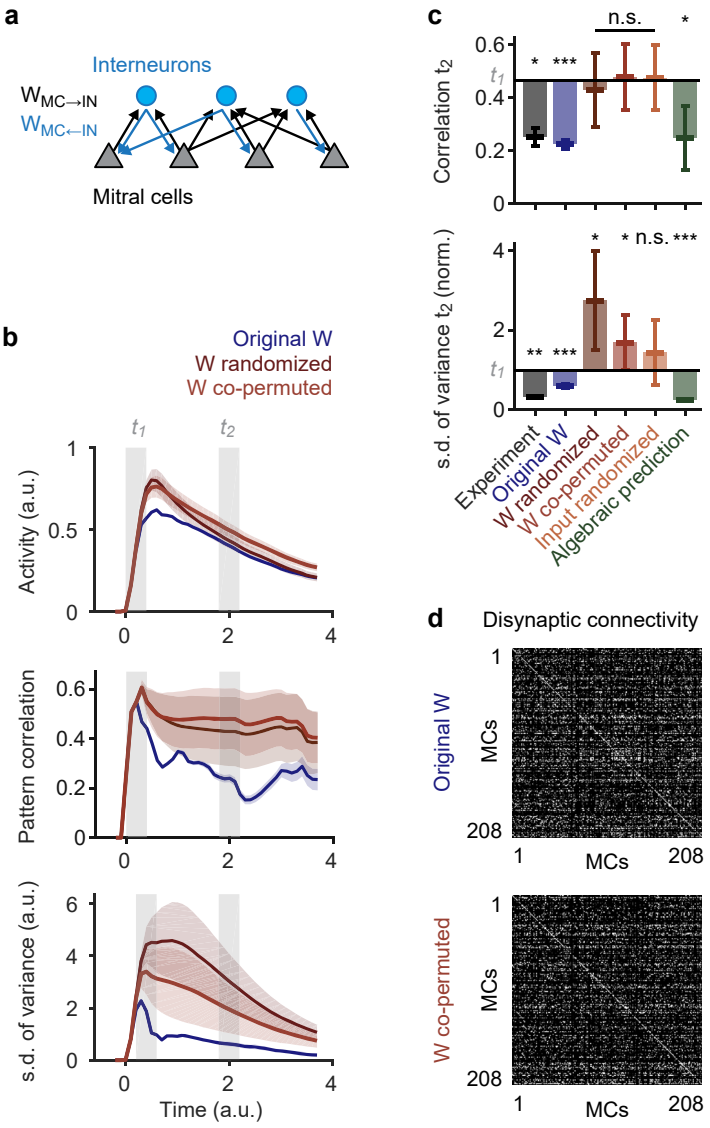

Fig. 3 | Whitening depends on connectivity. a, Architecture of simulated network with connections between MCs and INs. **b**, Time courses of simulated odor-evoked activity, pattern correlation and pattern variance obtained with different wiring diagrams. Blue: original wiring diagram obtained by circuit reconstruction. Dark red: fully randomized connectivity. Light red: co-permutation of feed-forward (MC→IN) and feed-back (MC←IN) connectivity. Shaded areas show s.d. across different permutations. **c**, Mean pattern correlation and s.d. of pattern variance at t_2. S.d. of pattern variance is normalized to the value observed experimentally at t_1. Horizontal black lines show mean experimental values at t_1. Statistical comparisons of correlation and s.d. of variance were performed using a Mann-Whitney U test and an F-test, respectively. For experimental results and simulations using the reconstructed wiring diagram error bars show s.d. across odor pairs (correlation; bile acids only) or individual odors (s.d. of variance). Significance tests compare values at t_2 to experimental values at t_1. For other simulation results, error bars show s.d. over 20 repetitions. Significance tests compare the mean over repetitions to the mean observed experimentally at t_1. *, $p < 0.05$; **, $p < 0.01$; ***, $p < 0.001$; n.s., not significant. **d**, Top: disynaptic connectivity matrix between MCs ($W_{MC\rightarrow IN} * W_{MC\leftarrow IN}$). Grayscale represents number of disynaptic MC-IN-MC connections (normalized). Bottom: example of a disynaptic connectivity matrix with the same order of MCs after co-permuting $W_{MC\rightarrow IN}$ and $W_{MC\leftarrow IN}$.

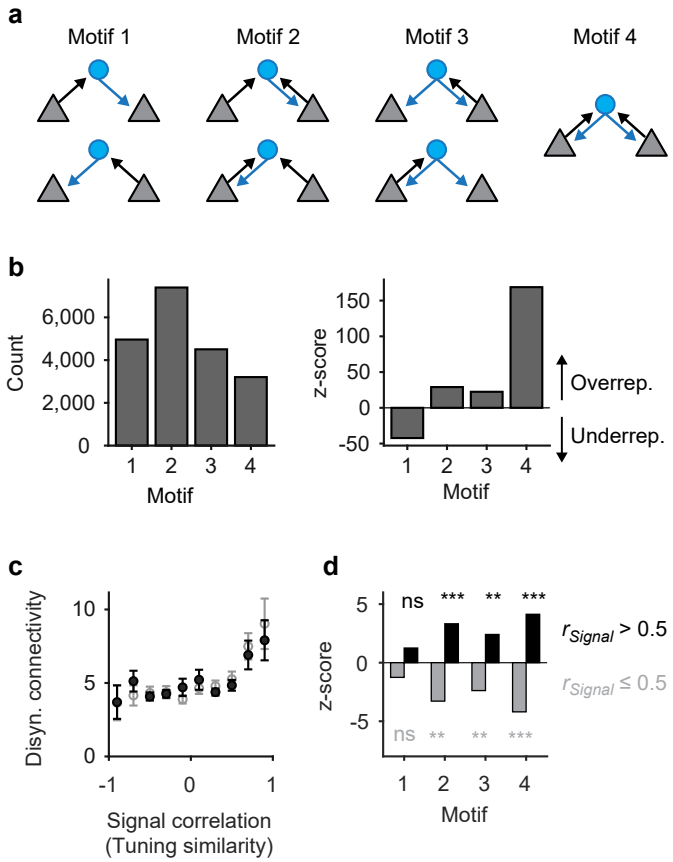

Fig. 4 | Tuning-dependent disynaptic connectivity in the OB. a, Classes of triplet connectivity motifs between MCs and INs. **b**, Left: number of connectivity motifs found in the wiring diagram (considering only MCs with activity measurements; n = 232). Right: z-score quantifying over- or under-representation of motifs as compared to 10,000 independent randomizations. **c**, Number of disynaptic connections between MCs as a function of tuning similarity (signal correlation; binned; mean ± s.e.m.). Black: all MCs (n = 21,528 pairs); gray: excluding MCs without at least one strong odor response (n = 7,875 pairs). **d**, Over- and under-representation of connectivity motifs among MC pairs with high signal correlation ($r_{Signal} > 0.5$; black) and among the remaining pairs ($r_{Signal} \leq 0.5$; gray).

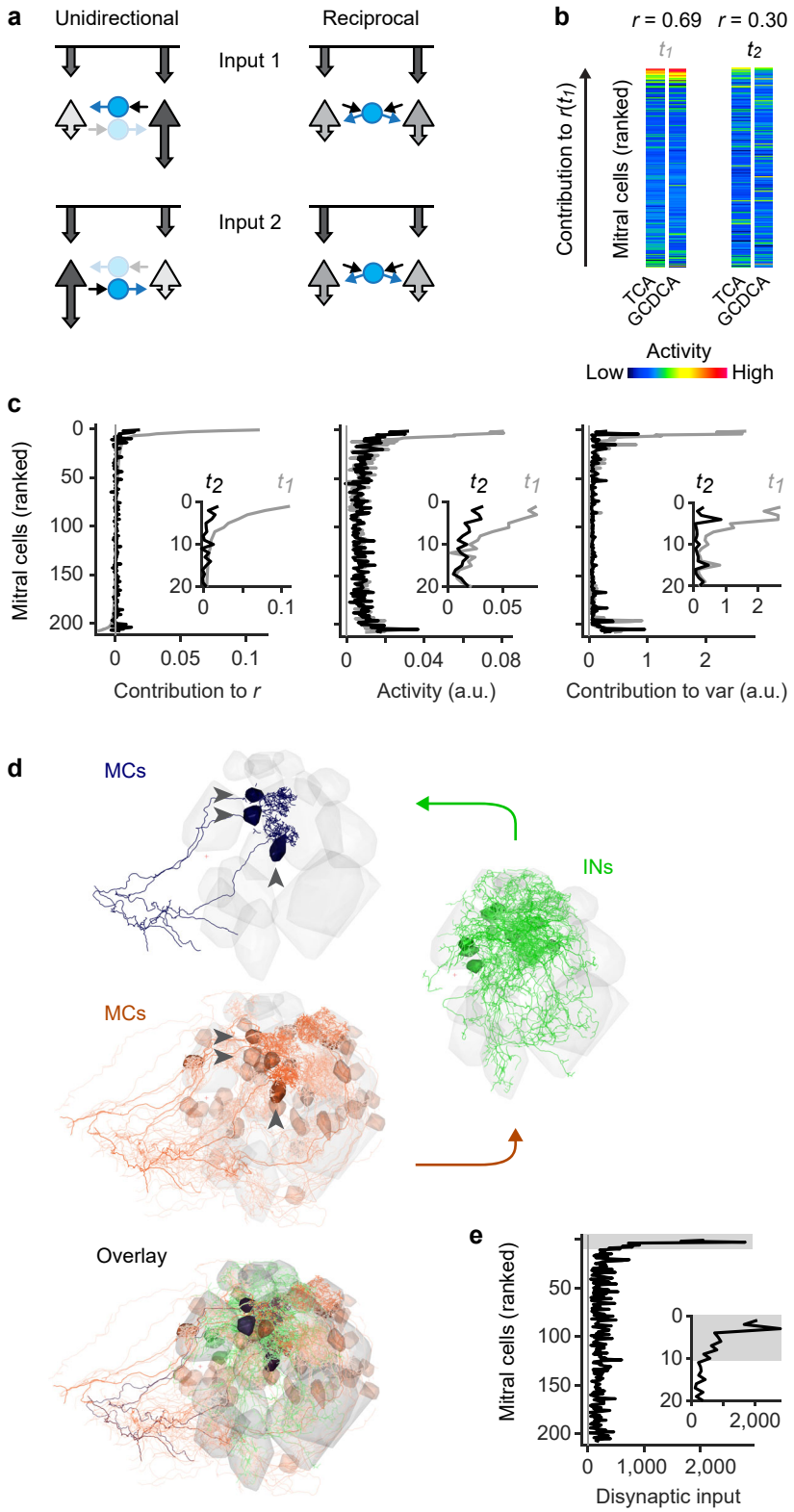

Fig. 5 | Disynaptic connectivity underlying feature suppression. a, Schematic illustration of contrast enhancement by unidirectional lateral inhibition (left) and down-scaling of cohort activity by reciprocal inhibition (right; feature suppression). Arrow length and grayscale indicate activity. **b**, Example of MC activity patterns evoked by two bile acids (TCA, GCDCA) that were decorrelated between t_1 and t_2. MCs are ranked from top to bottom by their individual contribution to the pattern correlation r at t_1 ($r_{i,t1}$). **c**, Left: average contribution of MCs to all pairwise correlations between activity patterns evoked by bile acids at t_1 and t_2. MCs were ranked by $r_{i,t1}$ for each pair of patterns as in **b**. Sorted vectors of correlation contributions were then averaged over odor pairs. Center, right: Mean bile-acid evoked activity of MCs and mean contribution of MCs to pattern variance. MCs were sorted by $r_{i,t1}$ and averaged as in the left panel. Gray and black curves show correlation contribution, activity, and variance contribution at t_1 and t_2, respectively (same sorting of individual neurons by $r_{i,t1}$ for all curves). Insets enlarge the top part of the curves (20 MCs with highest $r_{i,t1}$). **d**, Example of disynaptic retrograde tracing of functional cohorts in the wiring diagram. Blue: three MCs with highest $r_{i,t1}$ for the odor pair shown in **b** ("starter MCs"). Green: 12 INs with largest number of synaptic inputs to the starter MCs. Red: 48 MCs with largest number of disynaptic inputs to the starter MCs. Transparency represents the number of synaptic connections. Note that the MCs with strong disynaptic connectivity to the starter MCs include the starter MCs themselves, consistent with pronounced reciprocal connectivity among functionally related MC cohorts. **e**, Disynaptic MC-IN-MC connectivity as a function of correlation contribution at t_1 ($r_{i,t1}$; same ranking as in **b** and **c**). For each pair of bile acids, the 10 MCs with the highest $r_{i,t1}$ were selected as starter cells. Disynaptic inputs from all MCs were then represented in a vector and averaged over odor pairs. Note strong overrepresentation of disynaptic connectivity within the cohort of starter cells (gray shading).

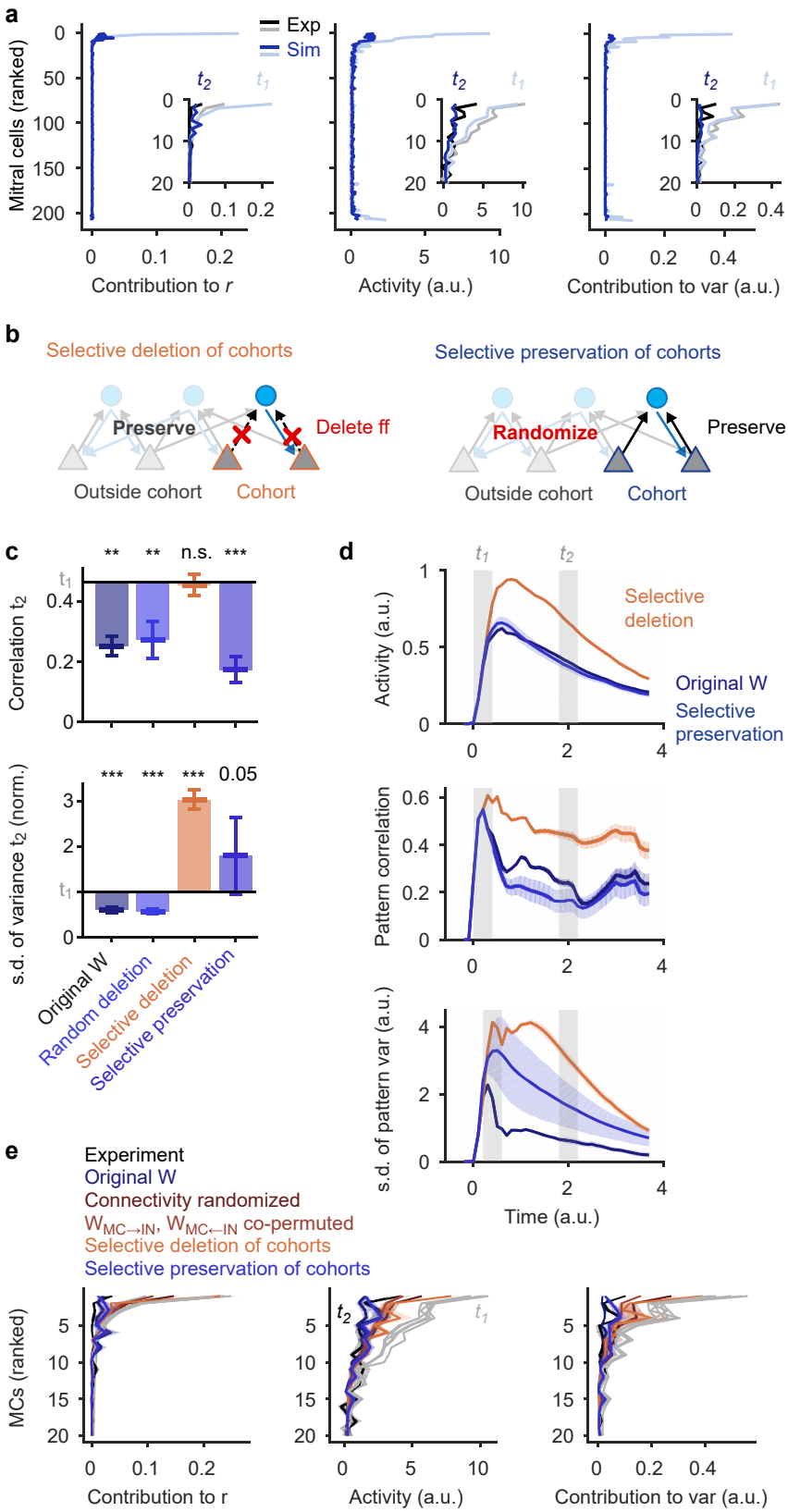

Fig. 6 | Mechanism of whitening analyzed by targeted manipulations of the wiring diagram. a, Mean correlation contribution, activity, and variance contribution of MCs responding to bile acids at t_1 (light blue) and t_2 (dark blue) in simulations. MCs were ranked by the correlation contribution $r_{i,tI}$ observed in experimental data as in **Fig. 5c**. Insets enlarge the top parts of the curves (20 MCs with highest $r_{i,tI}$) and compare simulation results to experimental data (gray, black) for the same 20 MCs. **b**, Schematic: selective deletion and selective preservation MC cohort connectivity in simulations. **c**, Mean pattern correlation and s.d. of pattern variance (normalized) at t_2 observed in simulations under different conditions. S.d. of pattern variance has been normalized to the experimentally observed value at t_1. Horizontal black lines show mean values at t_1; vertical bars show change relative to t_1. Statistical comparisons of correlation and s.d. of variance were performed using a Mann-Whitney test and an F-test, respectively. Error bars for original wiring diagram show s.d. across odor pairs (correlation; bile acids only) or individual odors (s.d. of variance); significance tests compare values at t_2 to experimental values at t_1. Other error bars show s.d. over means from 20 simulations and significance tests compare the mean over repetitions to the mean observed experimentally at t_1. **, $p < 0.01$; ***, $p < 0.001$; 0.05, $p = 0.05$; n.s., not significant. **d**, Time courses of pattern correlation and of the s.d. of pattern variance in simulations using different wiring diagrams. Shaded area shows s.d. across different permutations. **e**, Mean correlation contribution, activity, and variance contribution of the 20 MCs with the highest $r_{i,tI}$ observed experimentally and in simulations using different wiring diagrams. MCs were ranked by $r_{i,tI}$ observed in experimental data as in **a** and in **Fig. 5c** (same ranking under all conditions). Gray: t_1; Colored: t_2. Shading shows s.d. across 20 different permutations. Note that the reduction in correlation contribution, activity and variance contribution among MCs with high $r_{i,tI}$ is decreased when connectivity is modified globally or in functional cohorts, but not when connectivity of functional cohorts is preserved.

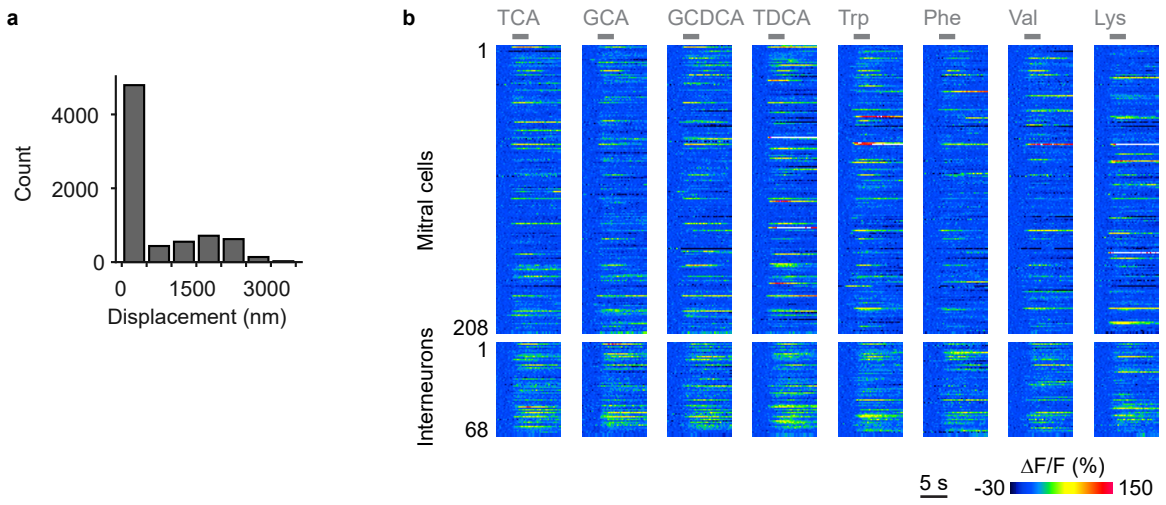

Supplementary Fig.1 | Mapping of datasets and activity measurements. a, Displacement of regions of interest (ROIs) during manual proofreading. ROIs representing somata were mapped from the EM dataset to optical image planes in each trial by an affine transformation that was determined by an iterative landmark-based procedure (Methods). Subsequently, the position of each ROI was adjusted manually on the optical image (n = 7,280 ROIs; six image planes with 11 trials each). The mean displacement (± s.d.) during manual adjustment (proofreading) was small (593 ± 833 nm), implying that automated mapping was highly reliable. **b**, Raw calcium signals (ΔF/F) evoked by eight odors in neurons that were present in all trials (208 MCs and 68 INs). Gray bars indicate odor stimulation.

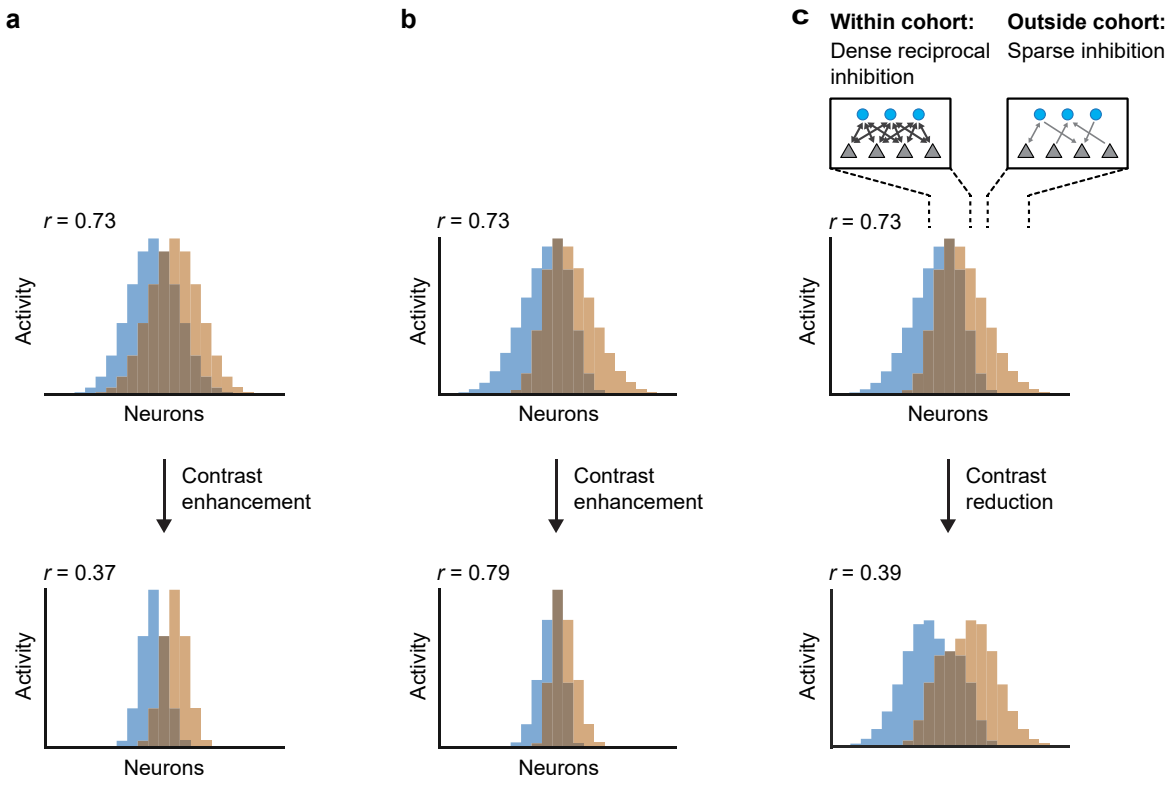

Supplementary Fig.2 | Effects of pattern transformations on pattern correlation. a, Effect of contrast enhancement on the correlation between displaced Gaussian patterns. In such patterns, strongly active units convey stimulus-specific information while weakly active units tend to be non-specific. Contrast enhancement therefore decorrelates patterns because it emphasizes strongly active units and suppresses weakly active units. **b**, Effect of contrast enhancement on the correlation between activity pattern that overlap in strongly active units. Contrast enhancement fails to decorrelate patterns because pattern-specific information is conveyed by moderately or weakly active units. **c**, Patterns that overlap in strongly active units are decorrelated by selective inhibition of strongly active units, which results in contrast reduction. Patterns are decorrelated because the relative contribution of moderately or weakly active units is enhanced. Selective inhibition of strongly active units is generated by dense reciprocal inhibition within cohorts of co-tuned neurons. Inhibitory feedback gain is therefore higher than the average inhibitory feedback gain within a co-tuned cohort when the stimulus feature that activates the cohort is present (feature suppression).